Design and Optimization of High Pressure Ratio Radial Inflow Turbine for Automotive Organic Rankine Cycle Waste Heat Recovery Application

Fuhaid Alshammari[a,b*], Apostolos Karvountzis-Kontakiotis[a], Apostolos Pesyridis[a], Ibrahim Alatawi[b]

[a] Brunel University London, Department of Mechanical, Aerospace & Civil Engineering, CAPF – Centre of Advanced Powertrain and Fuels, Uxbridge, UB8 3PH, United Kingdom

[b] University of Hail, Department of Mechanical Engineering, 81481, Hail, Saudi Arabia

Abstract

This paper presents a detailed design methodology of high pressure ratio radial inflow turbines integrated in Organic Rankine Cycles. The methodology is coupled with an optimization algorithm to optimize the input parameters specified by the designer. Moreover, a Design of Experiment technique is coupled to the design methodology to study the effect of each individual input parameter on the turbine performance. In addition, RefProP is implemented in the design methodology in order to account for the thermodynamic properties at the inlet and exit of each turbine stage. The maximum deviation between the current model and the test case was in the prediction of the rotor exit tip radius r_{5t} (which was used as input parameter in the test case) with a value of 5.38%. In addition, the model demonstrated the ability to optimize any existing radial inflow turbine. Based on the steady-state cycle simulation, a radial inflow turbine with a pressure ratio of 7 was designed for an automotive application and demonstrated a total-to-static efficiency and power output of 74.4% and 13.6 kW, respectively, for a 200kW-class engine.

Keywords: Organic Rankine Cycle; Radial Inflow Turbine; Optimization; Design of Experiment; Waste Heat Recovery; Internal Combustion Engine.

*Corresponding author: Fuhaid Alshammari
E-mail: Fu.alshammari@uoh.edu.sa

Nomenclature

Variables

1-5	Stations through turbine
a	Speed of sound [m/s]
A	area
b	blade height [m]
BK	Blockage factor [-]
C	Absolute velocity [m/s]
Cf	Friction factor [-]
Cm	Meridional velocity [m/s]
Cθ	Tangential velocity [m/s]
Ca	Axial coefficient [-]
Cr	Radial coefficient [-]
d	diameter [m]
h	Enthalpy [kJ/kg]
Ka	Discharge coefficient of the axial component [-]
Kr	Discharge coefficient of the radial component [-]
Ka,r	Cross coupling coefficient of the axial and radial components [-]
l	length [m]
M	Mach number [-]
m'	Mass flow rate [kg/s]
N	Rotational speed [RPM]
o	Throat opening [m]
P	Pressure [kPa]
Q	Volume flow rate (m3/s)
r	radius [m]
Re	Reynold number [-]
s	Entropy [kJ/kg.k]
T	Temperature [K]
U	Tip speed [m/s]
w	Relative velocity [m/s]
W	work [kW]
z	Axial length [m]

Subscript

b	back face
h	hub
hyd	hydraulic
opt	optimum
r	radial, rotor
rms	root mean square
s	insentropic, stator
t	tip, total
x	axial

Greek Symbols

μ	Viscosity [Pa.s]
η	Efficiency [-]
β	Relative angle [deg]
δ	Deviation angle [deg]
ε	Clearance [m]
ρ	Density [kg/m3]
α	Absolute flow angle [deg]
γ	Setting angle
ψ	Azimuth angle

Abbreviations

BSFC	Break specific fuel consumption
DoE	Design of experiment
DP	Design point
EoS	Equation of state
ICE	Internal combustion engine
NIST	National Institute of Standards and Technology
NOx	Nitrogen Oxide
OA	Optimisation Algorithm
ORC	Organic Ranke cycle
WHR	Waste heat recovery

1. Introduction

Commercial diesel engine manufacturers are under increasing pressure by public regulatory agencies to decrease pollutant and CO_2 emissions. State of the art vehicles embody both sophisticated after-treatment technologies to decrease exhaust pollutants and advanced combustion technologies for low CO2 emissions. However, the goal of over 50% brake thermal efficiency cannot be achieved with the currently existing technology without the utilization of some type of waste heat recovery technology, as the majority of the fuel energy is wasted [1].

Organic Rankine cycle (ORC) is considered as one of the crucial technologies to recover the wasted heat in low to medium heat sources due to the simplicity, availability of the components and reliability [2], [3]. Wang and Zhang [4] stated that the thermal efficiency of the combined system (six-cylinder diesel engine and ORC) can be increased by 13.69% combined with a reduction in bsfc by 15.86%. The analysis of Vaja and Gambarotta [5] demonstrated that a 12% increase in the overall efficiency can be achieved with respect to the engine when coupled to an ORC system. The ORC system is one operating on a Rankine cycle that uses organic fluid as the working medium instead of steam. Organic fluids possess lower boiling points than steam which make them more desirable in low temperature heat sources. However, ORCs have usually low thermal efficiency levels due to the low working temperatures of the organic fluids [6].

To avoid further reductions in efficiency levels, it is essential to select and design the appropriate expansion machine. The expander is the most important component in the ORC power plant as it is responsible for the power conversion. Comparing to positive displacement expanders, turbo-expanders offer many advantages such as compact structure, light weight and high efficiency [7]. Moreover, lubrication is not required when using turbo-machines which results in cheaper and less complex design [8]. According to the open literature, radial inflow turbines showed better performance in low to medium heat sources compared to axial ones [9], [10]. Such turbines are capable of achieving large enthalpy drops from a single stage while axial turbines require more stages to handle similar expansions. They are also more robust under increased blade loading, less sensitive to blade profile inaccuracies and easier to manufacture [11]. In the current study, the radial turbine was selected based on the detailed study by the authors which can be found in [6], [12].

Several well-known preliminary design methodologies are included in the open literature such as [13]–[17]. However, these conventional methodologies use ideal gas as the working fluid, resulting in non-optimum turbine design when real gases, such as organic fluids, are used. These methodologies also require some known parameters, such as flow angles and radii, which have a non-negligible effect on the efficiency of the design. In addition, such methodologies require a certain level of previous empirical knowledge [18]. Recently, radial inflow turbine as an expansion machine in ORC systems have been investigated in several studies such as [7], [19]–[21]. However, only the study by Rahbar et al. [7] focused on the details of design of the turbine. When comparing the current methodology with Rahbar et al. [7], the current model gives the opportunity for the designer to select one of three objective functions (turbine efficiency, power or size). In Rahber's model, on the other hand, the objective function is directly related to the cycle efficiency rather than the turbine efficiency. Rahbar et al. [7] studied the effect of dynamic turbine efficiencies on the cycle performance, rather than the constant turbine efficiency applied in most ORC studies. In addition, in the aforementioned models [7], [19]–[21], some thermodynamic properties were derived based on ideal gas correlations. However, as shown in Fuhaid et al. [22], the relative deviation for pressures within the range of the current study can be up to 40% when integrating ideal gas equations of state. Therefore, only real gas equations of state were applied in the current model. For the above reasons, the recent models [7], [19]–[21]were very brief ones with a lot of information missing which makes it difficult for the designer to the follow the process of the design. The current model presents a step-by-step design methodology for ORC radial inflow turbines. Moreover, a well-established stator model [23] was integrated in order to account for the expected supersonic flows at stator outlet due to high operating pressure ratios.

The current work is concentrated on the development of a design process of a full radial-inflow turbine stage based on certain input parameters. These parameters are optimized using an optimization technique integrated in the in-house code. In the optimization algorithm, which is a genetic optimization technique that eliminates the manual iterative procedure, the input parameters are considered and optimized as design variables to result in the optimum solution of the objective function. In a subsequent step, the optimized design variables are used as input parameters in the design code to estimate the performance and geometry of the turbine at the design point. Well-established models developed by the National Institute of Standards and Technology (NIST) (RefProP) [24] are integrated in the design procedure to account for the real gas properties. When the optimum design is achieved based on the optimization algorithm, a further investigation of the design variables is achieved using the Design of Experiment technique (DoE). The DoE is used to investigate the impact of each single input parameter on the whole design process while the other input parameters are kept constant. However, the designer also can investigate the influence of more than one parameter at the same time. The operating conditions at the volute inlet are specified by the steady-state model of the ORC to begin the mean-line methodology. Therefore, the designed turbine must match the operating conditions of the ORC model.

2. Powertrain Modelling

The proposed integrated powertrain model is schematically presented in Fig. 1. The input parameters of the model are the geometric characteristics of the heat exchanger (evaporator), the working fluid properties, the diesel engine maps and the expander performance. The model solution includes the calculation of the turbine power output, the ORC efficiency as well as the combined fuel consumption, NOx specific emissions and powertrain power output. Detailed results of the engine model can be found in [9].

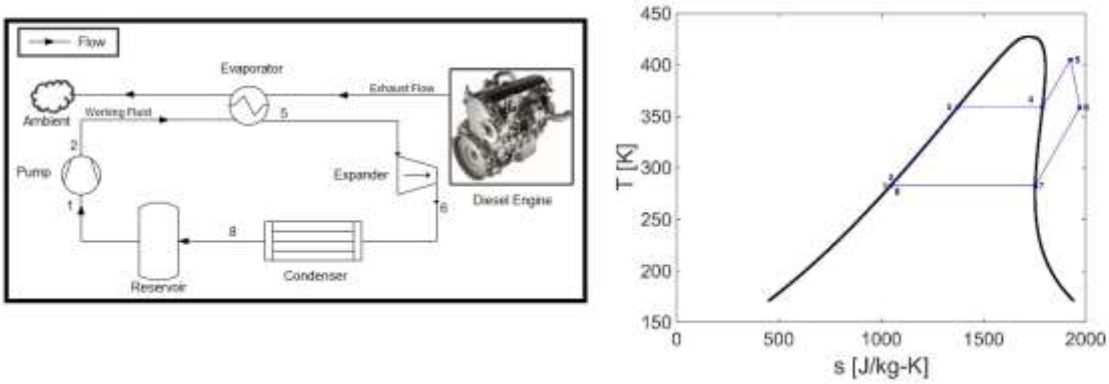

Fig. 1: Left) Schematic representation of the ORC powertrain; (Right) Schematic representation of the thermodynamic ORC cycle

2.1 Organic Rankine Cycle Modelling

An in-house MATLAB code has been developed for the thermodynamic modeling and optimization of the ORC system. The code utilizes RefProP to calculate the thermodynamic properties of the organic fluid at liquid and gaseous conditions. In this version of the ORC model, the system is optimized to operate at steady state conditions, while the heat exchanger is assumed ideal. In addition, for simplicity, the heat and pressure losses in the connecting pipes are neglected. The heat input from the exhaust gas is given by equations (1) and (2). The indexes are schematically described in the right section of Fig.1

$$\dot{Q}_{in} = \dot{m}_{wf}\,(h_5 - h_2) \qquad (1)$$

$$\dot{Q}_{exh} = \dot{m}_{exh}\,Cp_{air}(T_{exh,in} - h_{exh,out} \qquad (2)$$

The working fluid mass flow ($\dot{m}$), the ORC peak pressure (which controls the superheating percentage) and the exhaust temperature can be optimized from the in-house code, using the cycle thermodynamic efficiency as the objective function by fulfilling the constraints shown in (3). Regarding the rejected heat, it is assumed ideally that the exit temperature of the organic fluid is equal to 320K, and can be obtained using equation (4).

$$T_{exh,out} \geq 200^{o}C \qquad (3)$$

$$\dot{Q}_{out} = \dot{m}_{wf}\,(h_6 - h_8) \qquad (4)$$

The consumed power by the pump is determined by equation (5). The pump efficiency was assumed constant in this study and equal to 0.65, and was considered as a realistic value to reduce impact on the total ORC thermal efficiency calculation.

$$W_{pump} = \frac{\dot{m}_{wf}(P_2 - P_1)}{\rho_1 \eta_{pump}} \qquad (5)$$

The efficiency of the expander is given by the expander model through an interpolation and extrapolation module, as expander efficiency varies at different expander rotational speeds, pressure ratios and mass flow rates. Then the ORC model calculates the power produced by the expander through equation (6). The net electric power produced by the ORC is given by equation (7). The efficiency of the generator was assumed constant and equal to 0.92, while the mechanical losses are negligible, as the transmission ratio is 1:1 there are no gears between the expander and the generator.

$$\dot{W}_{expander} = \dot{m}_{wf}\,(h_5 - h_{6,is})\eta_{expander} \tag{6}$$

$$\dot{W}_{net} = \dot{W}_{epander} - \dot{W}_{pump} \tag{7}$$

$$\eta_{ORC} = \frac{W_{net}}{Q_{in}} \tag{8}$$

2.1 Engine Modelling

The engine model was based a Yuchai 7.25ℓ heavy duty diesel engine. It is a turbocharged, direct injection engine and fulfils the EURO III regulatory requirements. More details about the engine can be found in [25]. This engine appears to be a reasonable choice to apply a waste heat recovery system on, considering its high exhaust flow rate and the level of exhaust gas power available for conversion.

The modeling of this engine was performed using a commercial engine simulation tool (GT-Power), in order to develop the required engine maps. The final calibrated engine model calculates not only the fuel consumption, but also the exhaust gas temperature, the exhaust mass flow rate (exhaust waste heat) as well as the engine NOx emissions, which formation is based on a calibrat-ed extended Zeldovich mechanism sub-model.

3. Fluid Selection

Selection of working fluid for an ORC system is of key importance for the cycle efficiency and network. It also represents the first step in the design of an ORC. In ORC systems, only working fluids with low Global Warming Potential (GWP) and Ozone Depletion Potential (ODP) should be utilized.

Among the hundreds of fluids available, it is necessary to select either non-flammable fluids or flammable fluids whose auto-ignition temperature is higher than that of the exhaust gasses leaving the ICE. For example, only a small subset of the Alkanes can be considered. In particular, the Alkanes that have a flammability limit that is higher than the heat source of the ORC in question. In order to come up with the optimum fluid for the current applications, the authors [26] proposed novel method for the selection of the proper working fluid for ORC-WHR systems based on a radial expander in which thermodynamic properties and evaporator heat transfer surface are taken into account. The detailed results of the proposed method can be found in [26]. The final screening was based on the effect of the organic fluids on the required components of the ORC, namely,

- The evaporator heat transfer surface needs to be minimized due to the space constraints since this component has to be fitted into the immediate surroundings of the ICE exhaust manifold.
- The Radial turbine rotational speed is known to affect the turbine efficiency (furthermore, excessive rotational speeds lead to manufacturing and operational problems). The expander/turbine is directly coupled to the Power Conversion Unit (PCU), which performs the mechanical-electrical power conversion, and the alternator would become much more expensive.
- The Back work ratio (BWR), i.e., the ratio between pump and turbine power, must be minimized to maximize the cycle net power output.
- The Turbine external diameter should fall within the dimensional constraints of the retrofitting capability of the technology.

Based on the screened fluids in [26], NOVEC 649 was selected the working fluid for the current study. Table 1 presents the thermo-physical properties of the selected fluid.

Table 1*: Properties of the selected fluid (NOVEC 649).*

Fluid	$\boldsymbol{T_{cr}}$ $(\boldsymbol{K})$	$\boldsymbol{P_{cr}}$ $(\boldsymbol{bar})$	$\boldsymbol{P_{cr}}$ Kg/$\boldsymbol{m^3}$	Boiling Point (K)	Molecular Mass (g/kmol)	GWP	ODP
Novec649	441.81	18.69	606.8	322.2	316.04	1	0

4. Modelling of the Radial Inflow Turbine

Fig. 2 presents the full turbine stage. Radial-inflow turbines consist of three main components: volute, stator vanes and rotor blades. In some applications, a fourth component called diffuser is added to recover the otherwise wasted kinetic energy at the rotor exit and convert it into static pressure. The flow firstly enters the volute and is accelerated due to the reduced cross-section area in the stream-wise direction from 360° at the inlet to nearly 0° at the exit. Moreover, the tangential component of velocity increases before entering the nozzle vanes due to the reduced cross-section area, and flow is distributed evenly around the periphery of the stator inlet. After leaving the volute, the flow enters the stator vane where the fluid is further expanded and turned to enter the rotor blades in the optimum direction with the necessary tangential velocity. Finally, the fluid enters the most critical component of the turbine, which is the rotor, where the fluid is further expanded, converting the kinetic energy of the fluid into shaft power.

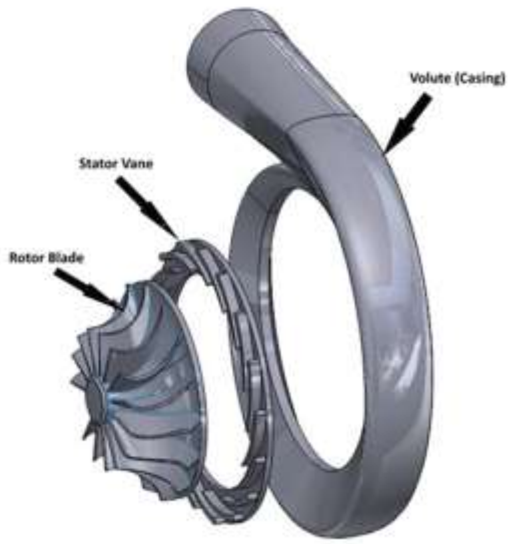

Fig. 2: Architecture of the radial turbine stage.

Fig. 3 presents a schematic meridional view of the turbine stage, and Fig. 4 presents the h–s diagram through the turbine stage.

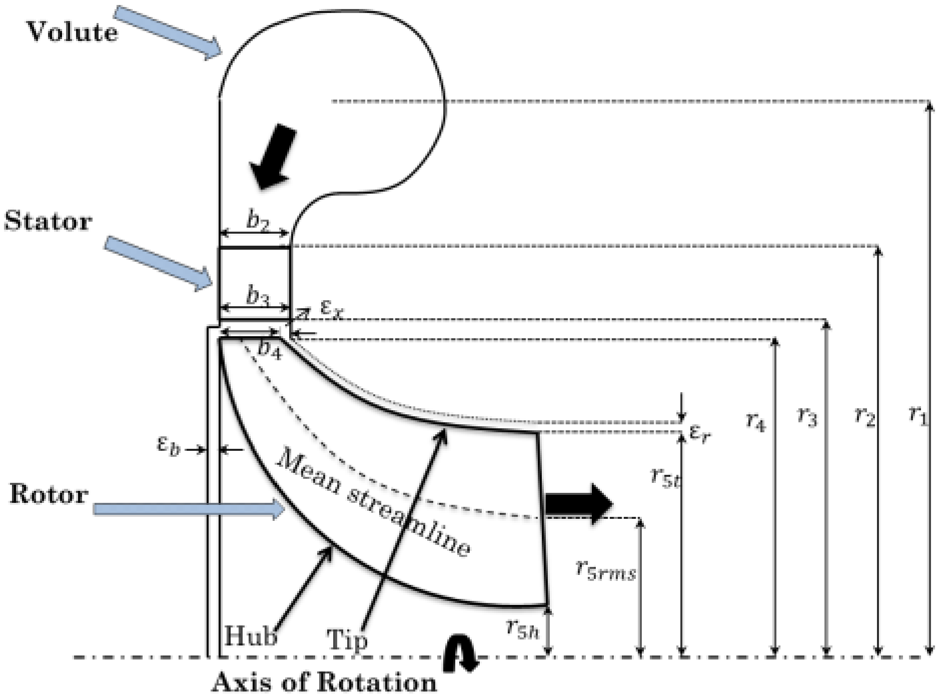

Fig. 3: Meridional view of the turbine stage.

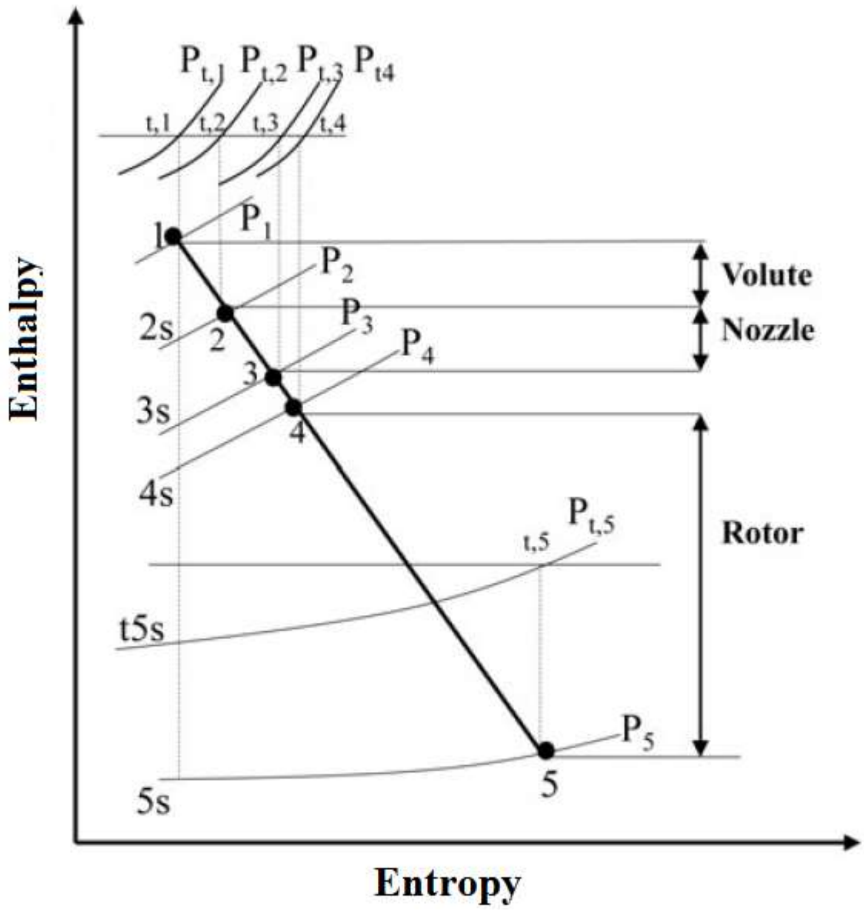

Fig. 4: Entalpy–Entropy diagram of the turbine stage.

4.1 Optimization Algorithm (OA)

An optimization technique is developed and coupled to the design procedure. The OA is essential because it is used to optimize the turbine and eventually to achieve better ORC performance. This code is a genetic optimization technique that eliminates the manual iterative procedure. The MATLAB optimization ToolboxTM® [27] is used to optimize the geometry and performance of the turbine under specified design conditions. This toolbox provides functions to maximize objective function and satisfy the user-defined constraints. It includes solvers for linear programming, mixed-integer linear programming, quadratic programming, nonlinear optimization and nonlinear least squares. Fmincon, which is a constrained nonlinear minimization or maximization algorithm, is the solver used in this study. This algorithm finds the constrained minimum of a scalar function of several variables at an initial estimate. The objective function is shown in equation (9).

$$\gamma = a_0\eta_{ts} + a_0 W_{out} + a_2 \frac{W_{out}}{d_{max}} \qquad (9)$$

The multipliers a_0, a_1 and $a_2$are used to define the objective function. Turbine total-to-static efficiency η_{ts}, expander power output W_{out} and the expander power over the turbine size $\frac{W_{out}}{d_{max}}$ are the important objective functions of the turbine. For example, if the turbine total-to-static efficiency η_{ts} is selected as the objective function, then the multipliers become as follows: $a_0 = 1$, $a_1 = 0$ and $a_2 = 0$. Different design criteria can lead to various optimized expander geometries. The flowchart of the optimisation algorithm is presented in Fig. 5. For brevity, the three terms in equation (9) are represented as F1, F2 and F3.

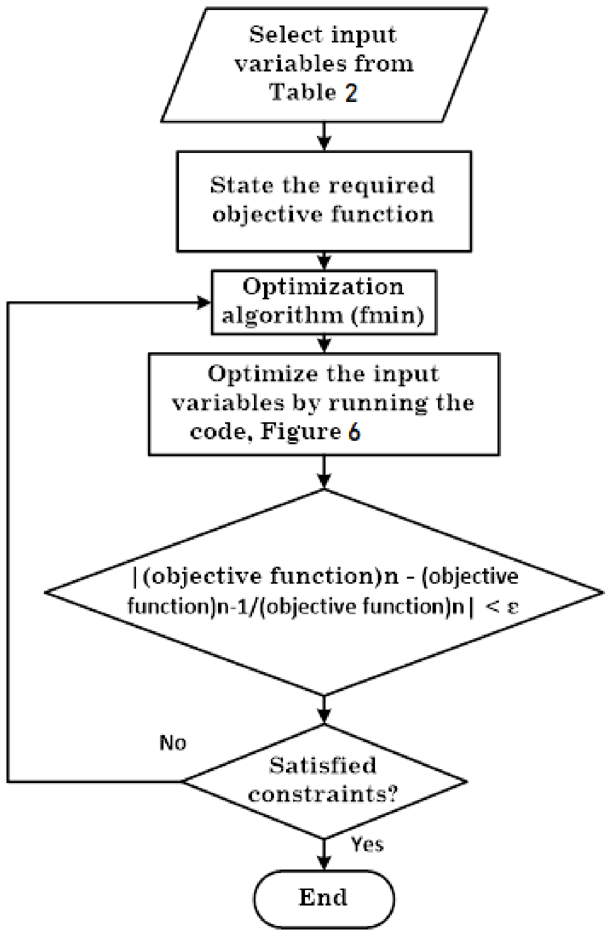

Fig. 5: Flowchart of the optimisation algorithm.

4.2 Design Point (DP)

This section presents the detailed procedure of the mean-line modelling at the design point. The DP code obtains the thermodynamic properties of the working fluid at each turbine stage (volute, stator and rotor) using the integrated real gas EoS and determines the geometric and performance parameters using the genetic optimization algorithm.

4.2.1 General Stage Modelling

For simplicity, fluid properties are assumed to be constant on a plane normal to its direction of motion. Therefore, these properties vary only along the mean streamline of the blade. Assuming the acceptable values of performance is common practice to proceed with the design. .

Table 2 presents the input parameters specified by the designer.

__Table 2__: Design Input Parameters.

Thermodynamic Inputs		Performance Input	
Parameters	Unit	Parameter	Unit
T_{01}	K	Ψ and φ	-
P_{01}	kPa		
P_5	kPa		
$\dot{m}$	Kg/s		

It is worth mentioning that the design code is an improved version of the design procedure presented by Moustapha et al.[13]. Fig. 7 presents the detailed flowchart of the proposed design methodology.

Considering that the stagnation temperature and pressure are given, the other thermodynamic properties can be easily found using EoS, as shown in equation (10). Equation (11) shows that $s_{5s} = s_{o1}$ based on the h–s diagram, Fig. 4. In addition, the isentropic pressure at the rotor exit P_{5s} is calculated from the given pressure ratio. Therefore, the isentropic enthalpy h_{5s} can be found using EoS, as shown in equation (11).

$$\{T_{01}, P_{01}\} = EoS(\rho_{01}, S_{01}, a_{01}, fluid) \quad (10)$$

$$\{P_{5s} = P_5, s_{5s} = s_{01}\} = EoS(h_{5s}, fluid) \quad (11)$$

Subsequently, the isentropic Δh_{is} and actual Δh_{act} enthalpies drops, and the turbine power output W_{out} can be obtained using the following equations:

$$\Delta h_{is} = h_{o1} - h_{5s} \quad (12)$$

$$\Delta h_{act} = \eta_{ts} \Delta h_{is} = h_{01} - h_{05} \quad (13)$$

$$W_{out} = \dot{m} \Delta h_{act} \quad (14)$$

4.2.2 Rotor Modelling

Rotor is the most significant component in the turbine stage because work transfer occurs in this region. Therefore, this component will be analysed first. The rotor is modelled based on two non-dimensional parameters, namely, loading coefficient Ψ and flow coefficient φ, as outlined by Moustapha et al. [13]. These parameters are shown in equations and .

$$\varphi = \frac{C_{m5}}{U_4} \tag{15}$$

$$\Psi = \frac{\Delta h_{act}}{U_4^2} \tag{16}$$

The rotational speed U_4 and the meridional velocity C_{m5} at the rotor outlet can be calculated because the loading coefficient Ψ and flow coefficient φ are imported from the optimization algorithm. Thus, the velocity triangle in Fig. 6 and the flow angles at the rotor inlet can be calculated.

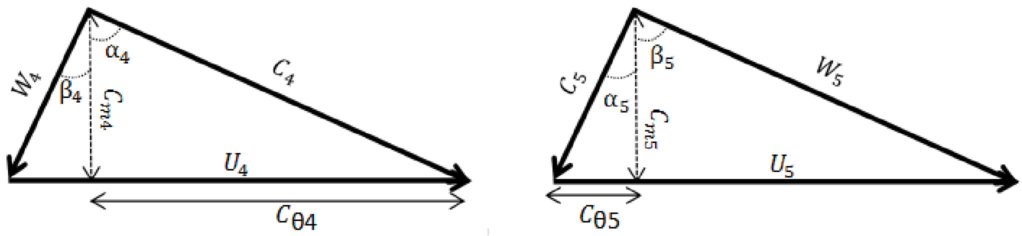

Fig. 6: Velocity triangles through the rotor.

Given that the absolute velocity at rotor inlet C_4 is now known, the static enthalpy h_4 can be calculated using the First Law of Thermodynamics. The $h - s$ diagram in Fig. 4 shows that $s_4 = s_{o4}$. To obtain s_{o4}, the stagnation pressure P_{o4} is calculated using equation (17) [23]. Therefore, all other stagnation properties, including s_{o4}, at the rotor inlet can be obtained using EoS at $\{h_{04} = h_{01}, s_4 = s_{04}\}$.

$$P_{o4} = P_{01} - \left[\frac{\rho_{o1} \Delta h_{act} (1 - \eta_{ts})}{4 \eta_{ts}}\right] \tag{17}$$

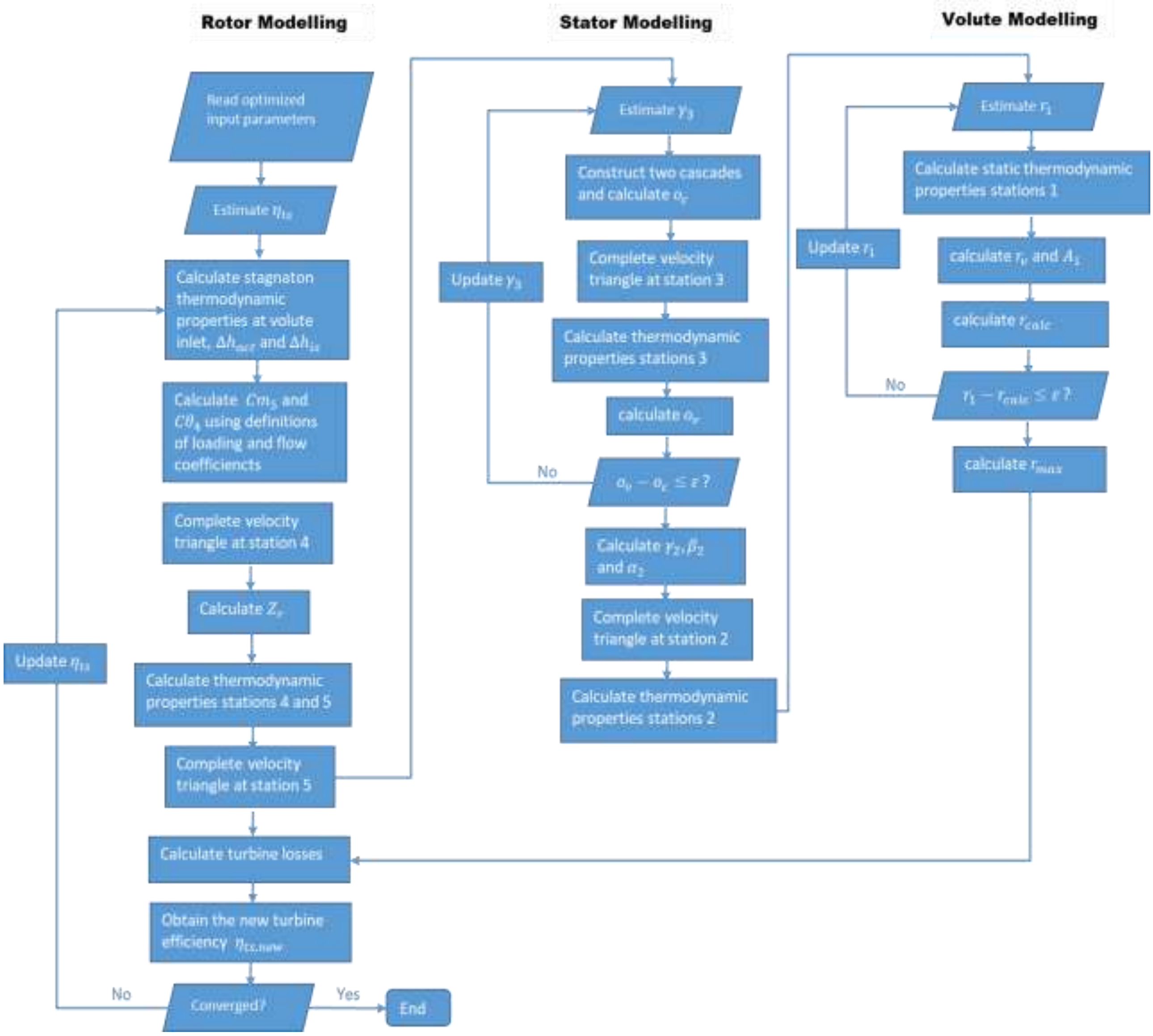

Fig. 7: Flowchart of the design point.

Consequently, the static thermodynamic properties at the rotor inlet can be found using the EOS at $\{h_4\ , s_4\}$, as shown in equation.

$$\{h_4, s_4 = s_{04}\} = EoS(\rho_4, P_4, T_4, a_4, fluid) \qquad (18)$$

According to the Euler equation, equation (19), the power output of the turbine increases with negative values of the exit swirl $C_{\theta 5}$. However, some reduction in efficiency will occur[14]. Therefore, $C_{\theta 5}$ is assumed to be zero to minimise the leaving loss of the rotor. One of the triangle parameters has to be obtained to complete the velocity triangle at the rotor exit. Aungier [23] proposed an effective procedure to estimate meridional speed C_{m5}, equation (20). When this equation is applied, the velocity triangle at the rotor exit can be obtained using trigonometry rules.

$$W_{output} = m^{\cdot}(U_4 C_{\theta 4} - U_5 C_{\theta 5}) \qquad (19)$$

$$C_{m5} = C_{m4}\left(1 + 5\left(\frac{b_4}{r_4}\right)^2\right) \qquad (20)$$

Subsequently, the static enthalpy h_5 is calculated using the First Law of Thermodynamics, as shown in equation (21), and the other thermodynamic properties are calculated using EoS, as shown in equation (22). Given that $s_{05} = s_5$, Fig. 4, the stagnation thermodynamic properties can be found using equation (23).

$$h_5 = h_{o5} + \frac{1}{2}C_5^2 \qquad (21)$$

$$\{h_5, P_5\} = EoS(\rho_5, T_5, a_5, s_5, fluid) \qquad (22)$$

$$\{S_{05}, h_{05}\} = EoS(\rho_{05}, T_{05}, a_{05}, P_{05}, fluid) \qquad (23)$$

To fully define the rotor geometry, the axial length and blade thickness of the rotor at its trailing edge are defined using equations (24) and (25), respectively [23]. The rotor mean throat o_5, which is the smallest distance between two adjacent blades, is calculated based on the value of the relative Mach number M_{5rel}, as shown in equation, (26) [23].

$$\Delta z = 1.5\,(r_{5t} - r_{5h}) \qquad (24)$$

$$t_{b5} = 0.02\, r_4 \qquad (25)$$

$$\begin{cases} o_5 = \dfrac{s_5 C_{m5}}{W_5} & for \quad M_{5rel} < 1 \\ o_5 = \dfrac{s_5 C_{m5} \rho_5}{\rho_* W_*} & for \quad M_{5rel} \geq 1 \end{cases} \qquad (26)$$

The blade angle of the rotor exit $\beta_{5,blade}$ can be obtained by the correlation shown in equation (27) as proposed by Suhrmann et al.[28], who stated that the correlation is based on the assumption that the relative flow angle β_5 is equal to $\beta_{5,blade}$ for zero mass flow, and the deviation δ_5 increases with mass flow.This equation is implicit in $\beta_{5,blade}$ and can be solved through the application of a bisection method. It is worth mentioning that this correlation is applied with ideal gases as the working fluid.

$$\frac{90-\beta_5}{90-\beta_{5,blade}} = 1 + \left(m^{\cdot} \frac{\sqrt{RT_{01}}}{P_5 D_4^2 (2\tan(90-\beta_{5,blade}) - 0.5)} \right)^{0.02(90-\beta_{5,blade})-0.255} \left(\frac{3\pi}{Z_r}\right) + 7.85 \frac{c_{rs}}{b_5} \tag{27}$$

4.2.3 Interspace Modelling

A small space between the stator trailing edge and rotor leading edge is essential for the nozzle wakes to mix out before entering the rotor [13]. However, the value of the interspace is a trade-off among reduced mechanical coupling, large-size turbine and increased pressure losses. The increase in interspace distance results in higher fluid friction and boundary layer, whereas reducing the interspace distance will result in lower blade row interaction [13]. In his CFD analysis, White [29] stated that the reduction of the total pressure from the stator trailing edge to rotor leading edge is 1.45%, which is sufficiently small to validate a constant total pressure in the interspace. Watanabe et al. [30] proposed a correlation to estimate a suitable clearance gap between the stator exit and the rotor inlet, as shown in equation, (28).

$$r_3 - r_4 = kb_3 cos\left(\frac{\alpha_3 + \alpha_4}{2}\right), \tag{28}$$

where b_3 is the stator blade height calculated using equation (29). ε_x and ε_r are the axial and radial tip clearances and given as a percentage of the exit blade height, equation (30).

$$b_3 = b_4 + \varepsilon_x \tag{29}$$

$$\varepsilon_x = \varepsilon_r = 0.04\, b_5 \tag{30}$$

4.2.4 Stator Modelling

To reduce incidence loss, the nozzle vanes must be set at an appropriate blade angle to enable a smooth swirl flow at the rotor leading edge. The design procedure of the nozzle vanes are performed iteratively, as shown in the flowchart, Fig. 7 . Li et al. [31] stated that the conservation of angular momentum can be applied in the vaneless space because the swirl coefficient between the stator exit and the rotor inlet is close to unity. Therefore, the tangential component of the velocity at the stator exit $C_{\theta 3}$ can be calculated, as shown in equation, (31).

$$C\theta 3 = \frac{C_{\theta 4} \cdot r_4}{r_3} \tag{31}$$

To construct the velocity triangle at the stator exit, the absolute velocity C_3 is calculated iteratively with a first assumption of $C_3 = C_{\theta 3}$. Subsequently, the static enthalpy h_3 is calculated from the total enthalpy and the kinetic energy, as shown in equation, (32).

$$h_3 = h_{o3} + \frac{1}{2} C_3^2 \tag{32}$$

The other thermodynamic properties can now be obtained, as shown in equation (33). Then, the new value of mass flow rate $\dot{m_{calc}}$ is obtained using equation (34), and the process is repeated until convergence is achieved.

$$\{S_3 = S_4, h_3\} = EoS(\rho_3, T_3, a_3, P_3, fluid) \tag{33}$$

$$\dot{m_{calc}} = 2\pi r_3 \rho_3 b_3 C_{m3} \tag{34}$$

Similar to the rotor throat width, the stator throat width is calculated using equation, (35) [23]. s_v is the vane pitch at the trailing edge. Moreover, it is related to the vane chord c_v , where $\frac{c_v}{s_v} = 1.2\ to 1.3$. This limit ratio is known as solidity σ, and it is implemented in the optimization algorithm to reach the optimum value within the limit. If the flow at the stator exit is supersonic ($M_3 \geq 1$), the nozzle throat width is calculated using the mass continuity equation between the throat passage and the exit station, as shown in, (35). $\rho_*\ and\ a_*$ are the density and speed of sound at sonic conditions, respectively.

$$\begin{cases} o_3 = s_v sin\alpha_3 \quad for \quad M_3 < 1 \\ o_3 = \dfrac{C_{m3}\rho_3}{\rho_* a_*} \quad for \quad M_3 \geq 1 \end{cases} \tag{35}$$

The number of nozzle vanes Z_s can be either calculated using equation (36) or defined by the user.

$$Z_s = \frac{2\pi r_3}{s_v} \tag{36}$$

The stator setting angle γ_3 should be calculated iteratively to set the required throat width. The stator vane is positioned at the stator outlet radius r_3 and rotated around the trailing edge with an initial guess of $\gamma_3 \geq 5^{\circ}$. Subsequently, the second vane is constructed by rotating the first vane around the origin by $\frac{2\pi}{Z_s}$, and the throat width will be the minimum distance between the two cascades. The iterative process is then repeated until convergence occurs at o_3. The radial chord length of the vane c_d is then calculated using equation.

$$c_d = c_v \cos \alpha_3 \tag{37}$$

Considering that the vane throat width o_3 is now known, cosine rule can be used to account for the change in angular momentum between vane throat and exit, as shown in equation (38). With the application of the conservation of momentum between stator throat and stator exit, static density can be calculated using equation (39).

$$\cos \alpha_{th} = \frac{o_3 Z_s}{2\pi r_3} \tag{38}$$

$$\rho_{th} = \rho_3 \frac{tan\alpha_{th}}{tan\alpha_3} \frac{r_{th}}{r_3} \tag{39}$$

Given that r_2 is calculated from the two cascades, the stator setting angle at the inlet γ_2 is obtained using equation (40). To calculate the velocity triangle at the stator inlet, an iterative process is essential to calculate the absolute velocity C_2 until convergence occurs at $m^{\cdot}$. The volute loss is calculated using equation (41) [13]. Consequently, the isentropic static enthalpy h_{2s} is calculated to obtain the rest of the thermodynamic properties at the stator inlet using equation (42). The static pressure P_2 and the rest of the thermodynamic properties are then obtained using EOS, as shown in equations (43) and (44), respectively. The new mass flow rate is then calculated using equation (45).

$$cos\gamma_2 = \frac{r_3 cos\gamma_3}{r_2} \tag{40}$$

$$\Delta h_{vol} = \frac{1}{2} k_{vol} C_2^2 \tag{41}$$

$$h_{2s} = h_2 - \Delta h_{vol} \tag{42}$$

$$\{h_{2s}, S_1\} = EoS(P_2, fluid) \tag{43}$$
$$\{h_2, P_2\} = EoS(\rho_2, T_2, a_2, s_2, fluid) \tag{44}$$
$$\dot{m}_{calc} = A_2 \rho_2 C_{m2} \tag{45}$$

4.2.5 Volute Modelling

Volute or the turbine inlet casing is used to distribute the fluid flow around the turbine periphery to provide a uniform mass distribution and uniform static pressure at the volute exit. An elliptical cross-section area is assumed due to the mathematical simplicity of ellipse calculations. Aungier [23] recommended a relationship between the ellipse semi-axes and the aspect ratio (AR), as shown in equation, (46). Therefore, the limit of AR is implemented in the optimization process to obtain the optimum value within the recommended limit.

$$0.75 \le AR \le 1.5 \tag{46}$$

Given that the volute radius is unknown, an iterative procedure is required with a first assumption of $r_1 = r_2$. Subsequently, equations (46) to (50) are solved iteratively until convergence is achieved.

$$C_1 = \frac{r_2 C\theta_2}{r_1 SC} \tag{47}$$

SC is the swirl coefficient that accounts for the effect of the wall friction in the volute. In some studies [14], [23], the value of SC is assumed to be equal to one. However, Moustapha et al.[13] stated that the analyses of radial turbine test data suggest a value in the limit of $0.85 < SC < 0.95$. In the current study, the value of SC is imported from the optimization process, where the value lies in the limit of $0.85 < SC < 1$.

$$h_1 = h_{01} - \frac{C_1^2}{2} \tag{48}$$
$$\{h_1, s_1\} = EoS(\rho_1, T_1, a_1, P_1, fluid) \tag{49}$$
$$A_1 = \frac{\dot{m}}{\rho_1 C_1} \tag{50}$$

4.2.6 Losses Model

The majority of losses in the turbine stage occurred in the rotor. The loss model of the rotor is based on a well-established model outlined in [28], [32]. Five main losses, namely, incidence, passage, tip clearance, windage and exit energy are included in the present model. Subsequently, rotor loss is calculated as the sum of the total losses of the rotor, as shown in equation, (51). Table 3 summarizes the losses through the turbine stage.

$$\Delta h_{loss,rotor} = \Delta h_{incidence} + \Delta h_{passage} + \Delta h_{tip} + \Delta h_{windage} + \Delta h_{exit} \tag{51}$$

***Table 3**: Radial Turbine Losses Modelling*

Type and correlation of losses	Equation
$\Delta h_{incidence} = \frac{1}{2}[W_4 \sin(\beta_4 - \beta_{4,opt})]^n$	*(52)*
$\Delta h_{passage} = \frac{1}{2}\left(2f_t \frac{L_h}{D_h}\bar{W}^2 + \frac{r_4 C_4^2}{r_c Z_r}\right)$	*(53)*
$\Delta h_{tip} = \frac{U_4^3 Z_r}{8\pi}\left(K_a \varepsilon_a C_a + K_r \varepsilon_r C_r + K_{a,r}\sqrt{(\varepsilon_a \varepsilon_r C_a C_r)}\right)$	*(54)*
$\Delta h_{windage} = k_f \frac{\bar{\rho} U_4^3 r_4^2}{2\dot{m}}$	*(55)*
$\Delta h_{exit} = \frac{1}{2} C_5^2$	*(56)*

The new efficiency is subsequently calculated, as shown in equation (57). The process is repeated until convergence is achieved.

$$\eta_{ts} = \frac{\Delta h_{act}}{\Delta h_{act} + \Delta h_{loss,volute} + \Delta h_{loss,stator} + \Delta h_{loss,rotor}} \tag{57}$$

4.3 Design of Experiments (DOE)

The indicator of the turbine quality is the total-to-static efficiency and power output. In addition, the turbine is part of a complete system that is used as a WHR system in ICEs. Moreover, the space in the interior of the vehicles is limited. Therefore, evaluating the size of the turbine is also important. The maximum size of the turbine is r_1 as shown in Fig. 3.

The DOE is a parametric study based on the simultaneous variation of one or more input parameters while the other input parameters are maintained constant. In each run, a single input parameter (or multiple) is varied while the other parameters are kept constant. Once the run is completed, the optimum value of the varied input parameter that leads to the optimum objective function is fixed. In the next run, another input parameter is varied and the process is repeated until the entire set of input parameters is examined.

5. Results and Discussion

5.1 Comparison with an Existing Model

The model is validated against a well-defined model, Glassman [17], to evaluate its accuracy. In Glassman's case [17], some significant inputs, such as power, rotational speed, stator exit angle, angular momentum distribution, rotor exit flow, specific heat ratio of the gas and stator radius ratios, must be specified by the designer to solve the model. This indicates that the designer has to have enough experience of empirical knowledge to specify the suitable input parameters. Therefore, the proposed methodology in this work requires substantially fewer input parameters, in which little or no experience of the empirical correlations is required. The results of both cases are compared in terms of geometry and performance of the turbine. Table 4 presents the design input parameters of the turbine presented in [17].

***Table 4**: Design Input Parameters [238]*

Parameter	Value	Unit
Fluid	Argon	-
Inlet stagnation temperature	1083.3	K
Inlet stagnation pressure	91	kPa
Exit static pressure	56.52	kPa
Rotational speed	38,500	rpm
Mass flow rate	0.277	Kg/s

The results of both cases are presented in Table 5, which clearly shows that the results of the current model are in good agreement with the test case (Glassman's model). In terms of turbine size, the current model overestimates the size, with 3.63% increase compared to the test case. The deviation in the turbine performance between the two models is 2.3%, indicating the overestimation of the current model. This result can be justified by the fact that the input parameters (φ, Ψ) in the current study are optimized for higher turbine performance. The maximum deviation between the two models is in the prediction of the rotor exit tip radius r_{5t} with a value of 5.38%. The results in Table 5 indicate that the results in the current model are in good agreement with the test case. Importantly, the model can optimize any existing turbine. It is worth mentioning that the test case is just a theoretical study and no experiment has been done to validate it.

***Table 5**: Comparsion between the Current Model and Glassman's Model.*

Parameter	Unit	Glassman	Current Model	Deviation %
Stator inlet radius $\boldsymbol{r_2}$	mm	97.75	101.3	3.63
Stator exit radius $\boldsymbol{r_3}$	mm	79.38	82.6	4.06
Absolute flow angle $\boldsymbol{\alpha_3}$	deg	72	73.7	2.36
Number of nozzle vanes $\boldsymbol{N_v}$	-	16	16	0.00
Rotor inlet radius $\boldsymbol{r_4}$	mm	78.74	76	3.48
Rotor exit hub radius $\boldsymbol{r_{5h}}$	mm	19.36	18.7	3.41
Rotor exit tip radius $\boldsymbol{r_{5t}}$	mm	55.42	58.4	5.38
Absolute flow angle $\boldsymbol{\alpha_4}$	deg	71.92	72.5	0.81
Relative flow angle $\boldsymbol{\beta_4}$	deg	−31.5	−33	4.76
Relative flow angle $\boldsymbol{\beta_5}$	deg	−70.69	−72	1.85
Number of rotor blades $\boldsymbol{N_r}$	-	12	12	0.00
Stage total-to-static efficiency $\boldsymbol{\eta_{ts}}$	%	83	85.3	2.3

5.2 .Parametric Study Using DOE

Fig. 8 presents the effect of flow coefficient φ on the performance of the turbine (power and efficiency), its maximum size, and Mach number at rotor inlet at different pressure ratios. Fig. 8 shows that the flow coefficient φ has a significant impact on the turbine total-to-static efficiency η_{ts} and overall turbine size r_1. The increase in flow coefficient φ is detrimental to the turbine total-to-static efficiency η_{ts} and beneficial to the turbine compact size. The definition of the flow coefficient implies that the increase of this parameter leads to higher meridional velocity at the rotor exit C_{m5} and, therefore, higher exit loss, as shown in equation (56). Fig. 8 depicts also the effects of flow coefficient φ on the turbine power output W_{out}, which decreases slightly as φ increases. This phenomenon can be justified by the definition of φ and Euler equation. As φ increases, the rotor blade speed U_4 decreases, thereby resulting in low power output. The effect of φ on the Mach number is insignificant because the two parameters have no direct relationship, as shown in Fig. 8. Fig. 8 also depicts the effect of turbine total-to-static pressure ratio PR_{ts} while increasing φ. The variation of PR_{ts} has remarkable effects on the investigated parameters. As PR_{ts} increases, the enthalpy drop through the turbine stage increases, leading to high turbine power output W_{out}. The increase in enthalpy drop leads to larger rotor diameter and, hence, larger turbine size r_1. The increase in the pressure ratio likewise leads to high Mach number M_4, where the flow becomes supersonic at $PR_{ts} \geq 5$.

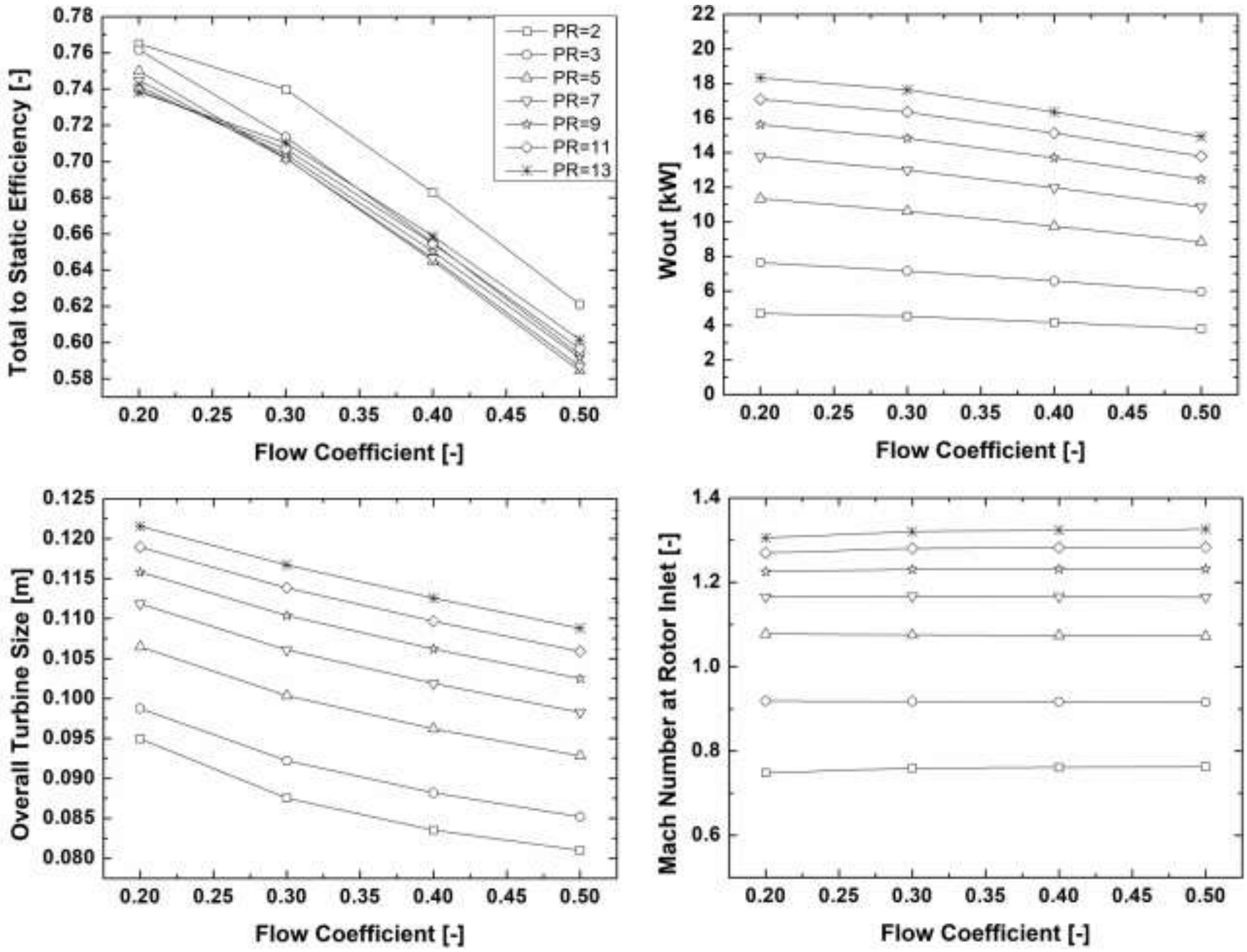

Fig. 8: Effect of flow coefficient φ on the investigated parameters.

Fig. 9 presents the effect of loading coefficient Ψ on the same parameters mentioned in the previous paragraph. Fig. 9 shows that the effect of Ψ has a slight significanceon η_{ts} and is insignificant on W_{out}. However, the results in Fig. 9 agrees well with Moustapha et al. [13], in which the turbine shows better performance with Ψ falling in the range of 0.8–1. Furthermore, loading coefficient Ψ has a significant effect on the turbine size and Mach number, as shown in Fig. 9. This phenomenon is directly related to the definition of the loading coefficient Ψ where the increase of Ψ leads to higher enthalpy drop and, therefore, a smaller diameter. The decrease of U_4 results in higher absolute velocity at the rotor inlet C_4, thereby leading to the higher Mach number M_4.

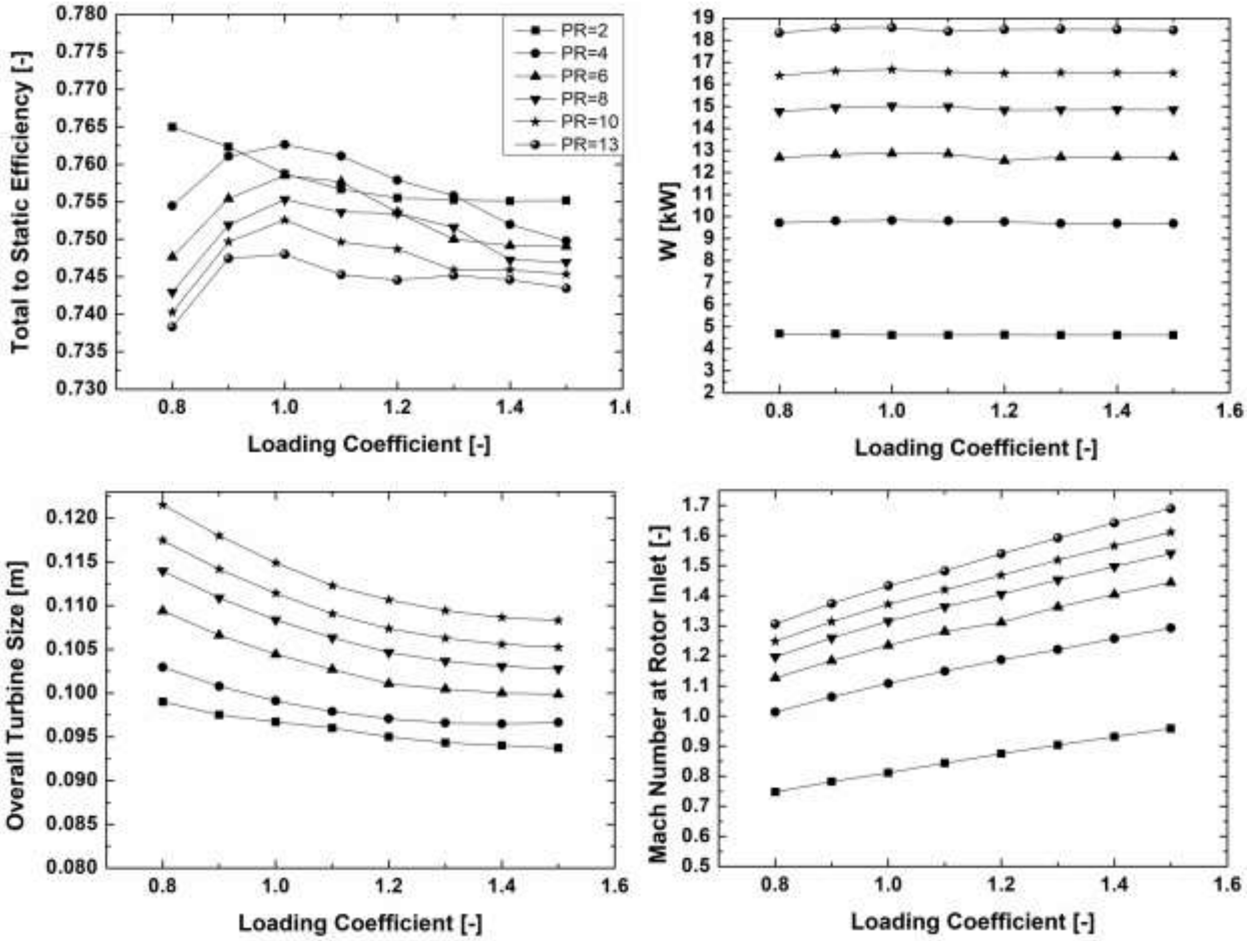

Fig. 9: Effect of loading coefficient Ψ on the investigated parameters.

Fig. 10 presents the effects of turbine rotational speed N on the four investigated parameters. The figure shows that the total-to-static efficiency η_{ts} increases gradually with the turbine speed N with an increase of 11.7% from 20,000 rpm to 70,000 rpm. In agreement with Euler equation, the turbine power output W_{out} presents the same trend as the η_{ts} with an increase of 12.5% from 20,000 rpm to 70,000 rpm. Fig. 10 also presents the effect of N on the two remaining parameters. The increase in turbine speed N is significantly beneficial to the turbine size r_1. As N increases, r_1 substantially decreases with a decrease of 27.14% from 20,000 rpm to 70,000 rpm. This observation can be justified by the definition of loading coefficient Ψ. For constant Ψ, the rotor radius r_4 is inversely proportional to the turbine speed N. This result also explains the increase in turbine efficiency η_{ts}, where the friction and exit loss decrease with turbine size. The effect of turbine speed on the Mach number M_4 of the rotor inlet is insignificant with a maximum increase of 1% from 20,000 rpm to 70,000 rpm.

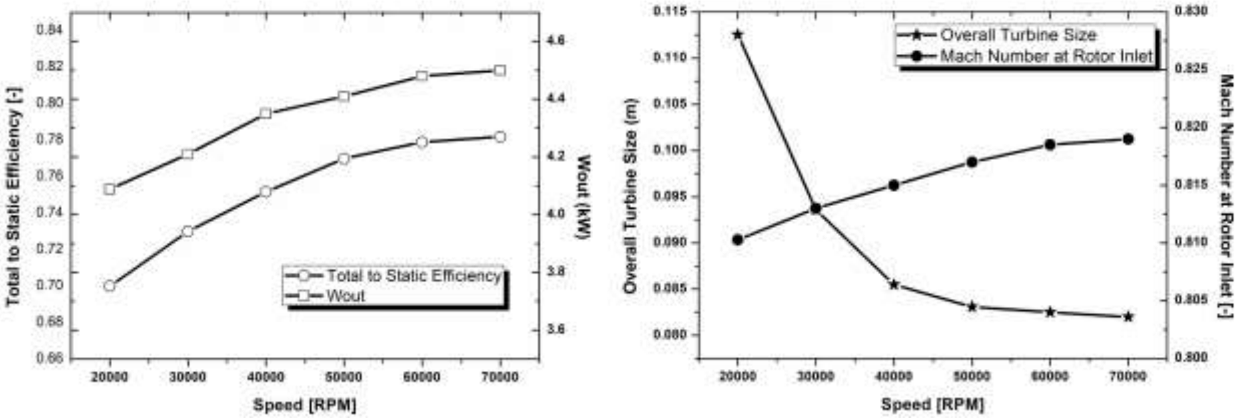

Fig. 10: Effect of rotational speed N on the investigated parameters.

Fig. 11 depicts the effect of working fluid mass flow rate on the four investigated parameters. Fig. 11 shows that W_{out} and η_{ts} increase substantially with the mass flow rate of the working fluid. This observation is directly related to the Euler equation. The figure also depicts the effect of the mass flow rate on turbine size r_1 and Mach number M_4. Clearly, the mass flow rate has a significant effect on the turbine size r_1 due to the increase in the enthalpy drop that leads to a larger turbine size. Similarly, M_4 increases substantially due to the increase in the enthalpy drop that leads to high rotor blade speed U_4. Therefore, a higher absolute velocity C_4 eventually results in higher M_4.

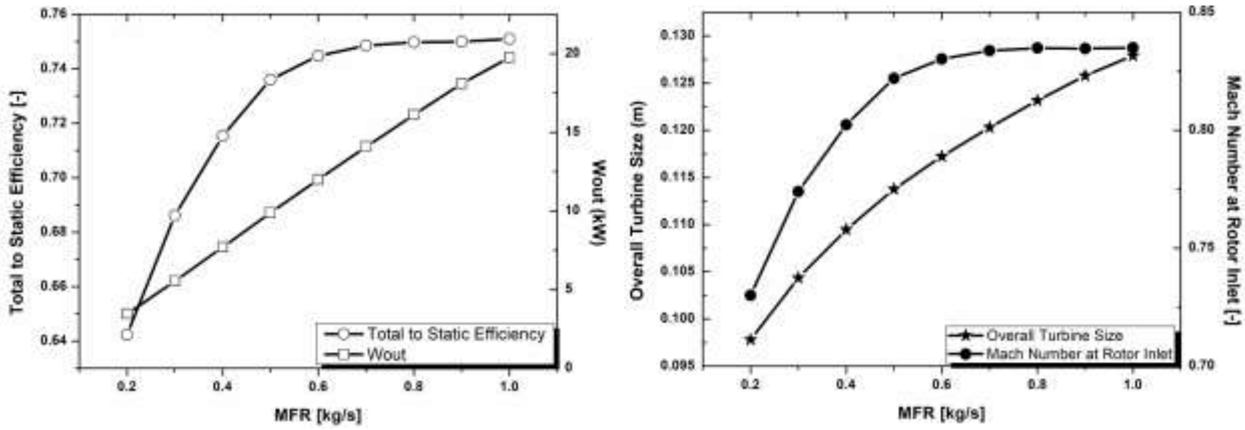

Fig. 11: Effect of mass flow rate MFR on the investigated parameters.

5.3 Design of the Optimum Turbine

The initial estimates of the input parameters presented in Table 6 are used to begin the optimization process. This model has three objective functions:

F_1: Total-to-static efficiency η_{ts}

F_2: Turbine power output W_{out}

F_3: Power density ${W_{out}}/{d_{max}}$

***Table 6**: Input Conditions of the Current Turbine*

Variable	Value	Unit
$\boldsymbol{P_0}$	900	KPa
$\boldsymbol{T_0}$	471.5	K
$\boldsymbol{P_5}$	128.5	KPa
N	40,000	rpm
$\boldsymbol{d_{max}}$	52	mm
$\dot{\boldsymbol{m}}$	0.8	Kg/s
Fluid	NOVEC 649	-

The results of the three objective functions are briefly presented in Fig. 12. The figure shows the results when F_1 is selected as the objective function. The optimum efficiency obtained is 74.4%, 71.8% and 70.1% when F_1, F_2 and F_3 are selected, respectively. The high value of F_1 is due to the low enthalpy losses shown in Fig. 13. The optimization of F_1 results in low absolute velocity at turbine exit C_5 and, hence, low exit loss. Moreover, the rotor speed U_4 and relative speed W_4 are the lowest, thereby resulting in lower tip clearance and incidence losses.

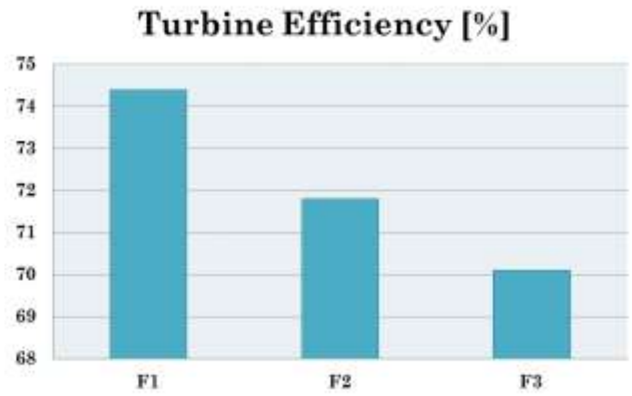

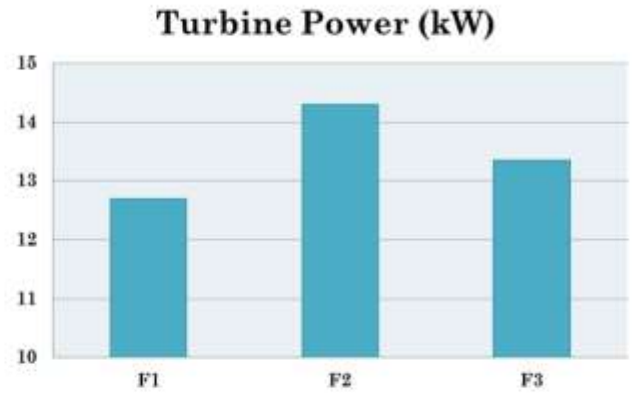

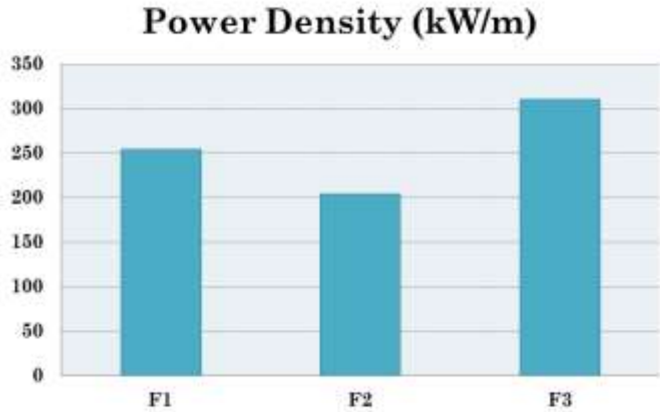

Fig. 12: Results of the OA using different objective functions.

Fig. 12 also presents the result when F_2 is selected as the objective function. The maximum power output W_{out} is 14.3 kW, and 12.7 kW and 13.36 kW when F_1 and F_3 are selected, respectively. This result is directly related to the Euler equation, where the mass flow rate and enthalpy drop Δh_{act} are the highest.

In addition, Fig. 12shows the result when F_3 is selected as the objective function. In some applications in which the size of the component is limited, this objective function is very crucial because higher turbine power and compact size are combined. The optimum value of F_3 is 310.7 kW/m; with turbine power and size are 13.36 kW and 0.043 m, respectively. The turbine size is substantially improved since its values are 0.05 m and 0.072 m for F_1 and F_2, respectively.

Fig. 13 presents the contribution of the rotor aerodynamic losses at the three objective functions. For the three objective functions, the secondary losses are dominant. This phenomenon is due to the high turning at the blade exit that results in efficiency deterioration. Tip clearance is the second dominant loss, which is expected with organic fluids. Organic fluids have large densities and low operating mass flow rates, leading to smaller blade height at the rotor leading edge b_4 and, therefore, large tip clearance.

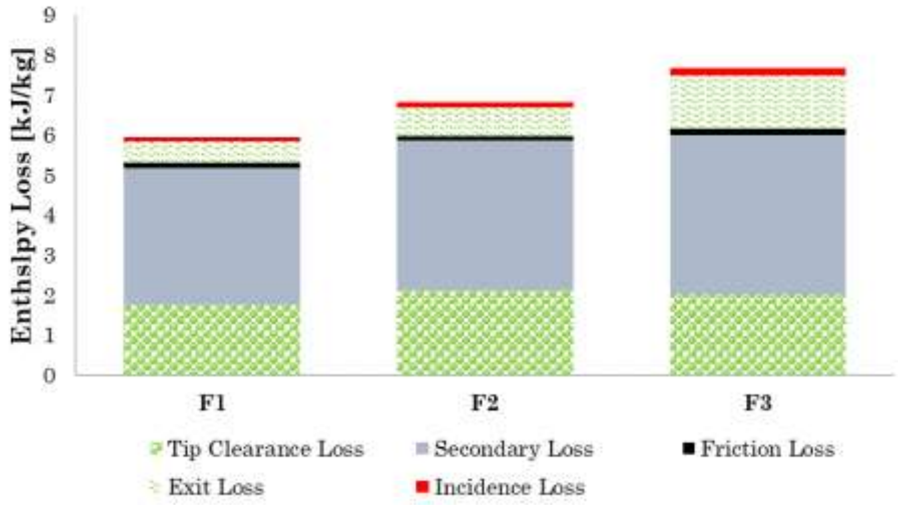

Fig. 13: Contributions of the rotor enthalpy losses on the performance of the turbine.

Table 7 shows the details of the final optimized radial-inflow turbine. The relative flow angle β_4 is positive, which is in contrast with conventional turbines where a negative angle is always present. This phenomenon is beneficial to maintain optimum incidence at the rotor inlet. Table 7 shows also that the Mach number at the stator exit M_3 is greater than unity, thus indicating supersonic flows. However, this result is expected due to the high pressure ratio ($PR = 7$). Moreover, organic fluids usually have low values for the speed of sound, which leads to supersonic regimes. At the rotor exit, the values of Mach numbers ($M_{5,rel}$ *and* M_5) are way below unity, that is, the likelihood of the creation of shock waves at this region is low.

***Table 7**: Detailed Geometry and Performance of the Optimized Turbine.*

Parameter	Value	Unit
	Volute: 1 Inlet 2: Exit	
r_1	0.0507	m
A_{th}	0.0004	m^2
	Stator: 2 Inlet 3: Exit	
M_2	0.17	$-$
M_3	1.35	$-$
r_2	0.044	m
r_3	0.0356	m
b_2	0.004	m
b_3	0.004	m
α_2	68.9	deg
α_3	79.4	deg
s_v	0.013	m
$\beta_{blade,2}$	76.3	deg
$\beta_{blade,3}$	66.7	deg
Z_s	17	$-$
o_v	0.0016	m

c_v	0.01	m
	Rotor: 4 Inlet 5: Exit	
M_5	0.45	
$M_{5,rel}$	0.58	
r_4	0.034	m
r_{5h}	0.008	m
r_{5t}	0.023	m
$r_{rms,5}$	0.017	m
b_4	0.003443	m
b_5	0.015	m
α_4	77	deg
α_5	10	deg
$\beta_{blade,4}$	54	deg
$\beta_{blade,5}$	-45	deg
N_r	15	$-$
z	0.0197	m
$\varepsilon_x = \varepsilon_r$	0.0005	m
	Performance	
N_s	0.5	$-$
R	0.46	$-$
v	0.642	$-$
η_{ts}	74.4	%
W_{out}	13.6	kW

6. Conclusion

This paper presented a full design methodology for a nozzled, high pressure ratio radial-inflow turbines integrated in ORC systems and applied to a real-world heavy-duty diesel engine. This methodology covered the preliminary and detailed aerodynamic design for the volute, nozzle vanes, and rotor blades. In addition, the proposed design methodology was linked with an optimization algorithm in order to obtain the best group of input parameters that eventually result in an optimum objective function, namely, the turbine efficiency, power or size. In order to investigate the effects of each input parameter individually, a design of experiment investigation was implemented. The proposed methodology can be widely applied to any nozzled or nozzle-less, radial-inflow turbine in order to achieve the critically important, high efficiency required of modern ORC turbo-expanders. In the future, the authors aim to validate the proposed model with experimental results using a built-in ORC system coupled to heavy duty diesel engine.

Acknowledgement

This work was supported by Innovate UK to this project [grant numbers. TS/M012220/1].

References

[1] T. V Johnson, "Review of Vehicular Emissions Trends," *SAE Int. J. Engines. 8(3)1152-1167, 2015, doi 10.4271/2015-01-0993.*, 2015.

[2] Y.-R. Lee, C.-R. Kuo, and C.-C. Wang, "Transient response of a 50 kW organic Rankine cycle system," *Energy*, vol. 48, no. 1, pp. 532–538, Dec. 2012.

[3] D. Fiaschi, G. Manfrida, and F. Maraschiello, "Thermo-fluid dynamics preliminary design of turbo-expanders for ORC cycles," *Appl. Energy*, vol. 97, pp. 601–608, Sep. 2012.

[4] J. Song and C. Gu, "Performance analysis of a dual-loop organic Rankine cycle (ORC) system with wet steam expansion for engine waste heat recovery," *Appl. Energy*, vol. 156, no. Supplement C, pp. 280–289, 2015.

[5] I. Vaja and A. Gambarotta, "Internal Combustion Engine (ICE) bottoming with Organic Rankine Cycles (ORCs)," *Energy*, vol. 35, no. 2, pp. 1084–1093, 2010.

[6] F. Alshammari, A. Karvountzis-Kontakiotis, A. Pesyridis, and M. Usman, "Expander Technologies for Automotive Engine Organic Rankine Cycle Applications," *Energies*, vol. 11, no. 7, 2018.

[7] K. Rahbar, S. Mahmoud, R. K. Al-Dadah, and N. Moazami, "Modelling and optimization of organic Rankine cycle based on a small-scale radial inflow turbine," *Energy Convers. Manag.*, vol. 91, pp. 186–198, 2015.

[8] Andreas P. Weiß, "VOLUMETRIC EXPANDER VERSUS TURBINE – WHICH IS THE BETTER CHOICE FOR SMALL ORC PLANTS," in *3rd International Seminar on ORC Power Systems, October 12-14, 2015, Brussels, Belgium*, 2015, pp. 1–10.

[9] A. Karvountzis-Kontakiotis *et al.*, "Effect of an ORC Waste Heat Recovery System on Diesel Engine Fuel Economy for Off-Highway Vehicles." 2017.

[10] F. Alshammari, A. Karvountzis-Kontakiotis, and A. Pesyridis, "Effect of radial turbo-expander design on off-highway vehicle organic Rankine cycle system efficiency," *Int. J. Powertrains*, vol. 7, no. 1–3, pp. 72–93, 2018.

[11] E. Sauret and A. S. Rowlands, "Candidate radial-inflow turbines and high-density working fluids for geothermal power systems," *Energy*, vol. 36, no. 7, pp. 4460–4467, 2011.

[12] F. Alshammari, A. Karvountzis-Kontakiotis, A. Pesiridis, and T. Minton, "Radial Expander Design for an Engine Organic Rankine Cycle Waste Heat Recovery System," *Energy Procedia*, vol. 129, pp. 285–292, Sep. 2017.

[13] H. Moustapha, M. F. Zelesky, N. C. Baines, and D. Japikse, *Axial and Radial Turbines*, 1st

ed. White River Junction: Concepts NREC, 2003.

[14] A. Whitfield and N. C. Baines, *Design of Radial Turbomachines*. Longman Scientific and Technical, Harlow, England, 1990.

[15] H. E. Rohlik, "Analytical Determination of Radial Inflow Turbine Design Geometry for Maximum Efficiency," *NASA TN D-4384*, 1968.

[16] C. Rodgers and R. Geiser, "Performance of a High-Efficiency Radial/Axial Turbine," *J. Turbomach.*, vol. 109, no. 2, pp. 151–154, Apr. 1987.

[17] A. Glassman, "Computer Program for Design Analysis of Radial-Inflow Turbines," NASA, Washington, D. C., USA., 1976.

[18] Carlos Ventura, "Aerodynamic Design and Performance Estimation of Radial Inflow Turbines for Renewable Power Generation Applications," Ph.D Thesis, The University of Queensland, 2012.

[19] H. E. Bekiloğlu, H. Bedir, and G. Anlaş, "Multi-objective optimization of ORC parameters and selection of working fluid using preliminary radial inflow turbine design," *Energy Convers. Manag.*, vol. 183, pp. 833–847, Mar. 2019.

[20] L. Zhai *et al.*, "An improved modeling for low-grade organic Rankine cycle coupled with optimization design of radial-inflow turbine," *Energy Convers. Manag.*, vol. 153, pp. 60–70, Dec. 2017.

[21] G. Lv, J. Yang, W. Shao, and X. Wang, "Aerodynamic design optimization of radial-inflow turbine in supercritical CO2 cycles using a one-dimensional model," *Energy Convers. Manag.*, vol. 165, pp. 827–839, Jun. 2018.

[22] F. Alshammari, A. Karvountzis-Kontakiotis, A. Pesiridis, and P. Giannakakis, "Off-design performance prediction of radial turbines operating with ideal and real working fluids," *Energy Convers. Manag.*, vol. 171, pp. 1430–1439, Sep. 2018.

[23] R. H. Aungier, *Turbine aerodynamics: Axial-flow and radial-inflow turbine design and analysis*, 1st ed. New York, 2006.

[24] E. Lemmon, M. Huber, and M. McLinden, "NIST Standard Reference Database 23: Reference Fluid Thermodynamic and Transport Properties-REFPROP, Version 9.0, National Institute of Standards and Technology, Standard Reference Data Program, Gaithersburg, Maryland, USA." 2010.

[25] F. Alshammari, A. Pesyridis, A. Karvountzis-Kontakiotis, B. Franchetti, and Y. Pesmazoglou, "Experimental study of a small scale organic Rankine cycle waste heat recovery system for a heavy duty diesel engine with focus on the radial inflow turbine expander performance," *Appl. Energy*, vol. 215, pp. 543–555, Apr. 2018.

[26] B. Franchetti, A. Pesiridis, I. Pesmazoglou, E. Sciubba, and L. Tocci, “Thermodynamic and technical criteria for the optimal selection of the working fluid in a mini-ORC,” in *Proceedings of ECOS 2016 - The 29th International Conference On Efficiency, Cost, Optimization, Simulation and Environmental Impact of Energy Systems*, 2016.

[27] The MathWorks, “MATLAB and Statistics Toolbox Release 2014b.” 2014.

[28] J. F. Suhrmann, D. Peitsch, M. Gugau, T. Heuer, and U. Tomm, “Validation and Development of Loss Models for Small Size Radial Turbines,” no. 44021. pp. 1937–1949, 2010.

[29] M. White, “The design and analysis of radial inflow turbines implemented within low temperature organic Rankine cycles,” PhD thesis. City University London, 2015.

[30] I. Watanabe, I. Ariga, and T. Mashimo, “Effect of Dimensional Parameters of Impellers on Performance Characteristics of a Radial-Inflow Turbine,” *J. Eng. Power*, vol. 93, no. 1, pp. 81–102, Jan. 1971.

[31] S. Li, E. M. Krivitzky, and X. Qiu, “Meanline Modeling of a Radial-Inflow Turbine Nozzle With Supersonic Expansion,” no. 49729. p. V02DT42A036, 2016.

[32] N. C. Baines, “Radial Turbines, an integrated design approach,” in *6th European conference on Turbomachinery- Fluid Dynamics and Thermodynamics.*, 2005.